Composite Structures 237 (2020) 111867

Contents lists available at ScienceDirect

Composite Structures

journal homepage: www.elsevier.com/locate/compstruct

# Mechanics of bioinspired functionally graded soft-hard composites made by multi-material 3D printing

M.J. Mirzaali[a,*], A Herranz de la Nava[a], D. Gunashekar[a], M. Nouri-Goushki[a], R.P.E. Veeger[a], Q. Grossman[b], L. Angeloni[a,c], M.K. Ghatkesar[c], L.E. Fratila-Apachitei[a], D. Ruffoni[b], E.L. Doubrovski[d], A.A. Zadpoor[a]

[a] Department of Biomechanical Engineering, Faculty of Mechanical, Maritime, and Materials Engineering, Delft University of Technology (TU Delft), Mekelweg 2, 2628 CD Delft, the Netherlands
[b] Mechanics of Biological and Bioinspired Materials Laboratory, Department of Aerospace and Mechanical Engineering, University of Liège, Liège, Belgium
[c] Department of Precision and Microsystems Engineering, Faculty of Mechanical, Maritime, and Materials Engineering, Delft University of Technology, Mekelweg 2, 2628CD Delft, the Netherlands
[d] Faculty of Industrial Design Engineering (IDE), Delft University of Technology (TU Delft), Landbergstraat, 15, 2628 CE Delft, the Netherlands

ARTICLE INFO

*Keywords:*
Multi-material 3D printing
Fracture toughness
Hard-soft interfaces
Functionally graded materials

ABSTRACT

Functional gradients are material transitions that are found in nature and are known to result in materials with superior properties and multiple functionalities. The emerging multi-material 3D printing (=additive manufacturing, AM) techniques provide a powerful tool for the design and fabrication of bioinspired functionally graded materials (FGMs). In particular, the spatial distribution of materials can be controlled at the level of individual volumetric pixels (voxels *i.e.*, cubes with side lengths of 20–40 μm), thereby ensuring accuracy, reliability, and reproducibility of the obtained properties and allowing for systematic studies of how various design variables affect the deformation and fracture behaviors of FGMs. Here, we designed, 3D printed, and mechanically tested tensile and notched FGMs specimens with step-wise (*i.e.*, 5-, 10-, and 15-steps) and continuous (sigmoid and linear) gradients. The deformation and fracture mechanisms of these FGM composites were studied using digital image correlation, digital microscopy, and scanning electron microscopy. We further characterized the chemical composition and local mechanical properties of FGM composites using XPS and nanoindentation measurements, respectively. Tensile test specimens with a continuous gradient (*i.e.*, linear) exhibited much higher Young's moduli (≈3-folds) and ultimate strengths (≈2-folds) but lower elongations (≈2-folds drop) as compared to those with stepwise gradients (*i.e.*, 5-steps). Similarly, notched specimens with linear gradients exhibited 2-folds higher values of the stiffness and fracture stress, but 1.5-folds lower fracture strains as compared to those with 5-steps gradients. Although we found non-uniform highly concentrated strain distributions in all specimens, FGMs with linear gradients showed a smoother strain distribution and smaller crack blunting zones as compared to those with stepwise gradients. Our results imply that for stiffness and strength linear-gradient perform better than abrupt hard-soft-hard specimens.

## 1. Introduction

Throughout the history of the design and fabrication of advanced functional materials, nature has been a constant source of inspiration. One of the areas of inspiration is how nature excels at creating hard-soft interfaces. Various types of internal and external interfaces exist in biological systems [1,2], which support specific functions and exhibit particular properties. Some of these important functions and properties improve the fracture resistance (*e.g.*, soft interfaces introduced by protein layers within hard mineral tablets placed in a brick-and-mortar fashion in nacre [3]), or to allow the materials to deform or move easily upon application of external stimuli (*e.g.*, motion of pine cone under humid/dry conditions [4]), or to bridge/join two materials with similar/dissimilar properties (*e.g.*, dentine-enamel connection in teeth [5] and the attachment of ligaments and tendons to bone [6]). Different strategies can be found in biological materials to mitigate the stress concentrations at the interfaces including gradual changes either in the chemical compositions or microstructural features across the interfaces. Examples are the gradual changes from stiff to compliant materials in the squid beaks [7] or the change in the porosity between trabecular

* Corresponding author.
*E-mail address:* M.J.MirzaaliMazandarani@tudelft.nl (M.J. Mirzaali).

https://doi.org/10.1016/j.compstruct.2020.111867
Received 3 March 2019; Received in revised form 24 December 2019; Accepted 2 January 2020
Available online 03 January 2020
0263-8223/ © 2020 Elsevier Ltd. All rights reserved.

and cortical bones [8].

In addition, joining two hard materials via a flexible connector frequently occurs in load-bearing tissues and organs such as articular cartilage [9,10], ligaments [11], and intervertebral disks [12,13]. These viscoelastic collagenous connective tissues are responsible for articulation, shock absorption, friction reduction, and facilitation of load transmission between two hard tissues (*i.e.*, bones) under different physiological loading scenarios (*e.g.*, walking, jumping, pivoting, *etc.*) [14,15]. In addition to physical and microstructural differences among these soft connective tissues, a common (gradual) zonal compositional variation can be found in their extracellular matrixes (ECM) to support the biomechanical functionality.

The above-mentioned strategies can be implemented in the design and fabrication of advanced bioinspired functionally graded materials (FGMs) [16–22]. One relevant example is the design of biomimetic engineered graft scaffolds [23–25] in the field of interface tissue engineering to create graded biomaterials that properly adjust the mechanical stresses to facilitate effective tissue integration at joints with different tissue types [26].

Biomimetic graded natural or synthetic polymers (*e.g.*, hydrogels and nanofibers) have been fabricated in the past using conventional manufacturing methods such as particulate leaching [27], electrospinning [28], magnetic actuation [29–31] and phase separation [32]. However, these methods have inherent limitations that strongly limit our ability to precisely control the spatial distribution of properties. The advent of additive manufacturing (AM, = 3D printing) techniques including selective laser sintering (SLS), fused deposition modeling (FDM), 3D bioprinting [33], and inkjet bioprinting [34] has created a host of new opportunities for the design and fabrication of advanced functional materials. In particular, multi-material AM techniques (*e.g.*, inkjet bitmap 3D printing [35]) have provided unparalleled opportunities for the development of biomimetic polymeric FGM composites with precise control over the spatial distribution of properties at ultrafine resolutions [36–39]. Moreover, multi-material AM techniques enable fabrication of reliable, reproducible, and potentially cost-effective products that could exploit the favorable properties of advanced FGMs to create functionalities that are hard or impossible to achieve using conventional fabrication techniques. Such bioinspired FGMs have numerous potential applications in high-tech industries such as automotive, soft robotics, aerospace, and energy [16,17,20,40,41].

One of the advantages of FGMs over conventional materials is that by engineering the functional gradient at the interface of hard-soft attachments, one can prevent the typical failure mechanisms such as delamination in traditional composites [42]. Several parameters can influence the properties of FGMs, including the types of the gradient (*i.e.,* continuous or discontinuous) and its dimensions [43,20]. Through independent adjustment of each of those parameters, the properties of FGMs can be tailored. Therefore, it is necessary to systematically study the different design parameters and their effects on the properties of FGMs. Moreover, the accuracy and efficiency of the current fabrication methods in achieving such properties need to be justified. In this study, using polyjet 3D printing and by implementing several characterization methods at different length-scales, we aimed to investigate the properties of some of the relevant classes of FGMs.

## 2. Material and methods

In order to use FGMs as structural materials, it is necessary to understand their mechanical properties and fracture behavior under different loading conditions. Here, we studied the mechanical properties and fracture behavior of functionally graded soft-hard polymeric composites. We designed, additively manufactured, and mechanically tested two groups of FGM specimens with step-wise (*i.e.*, 5-steps, 10-steps, and 15-steps, Fig. 1a–c) and continuous (sigmoid and linear, Fig. 1e and f) gradients. An advanced voxel-based multi-material AM technology (Objet350 Connex3™ 3D printer, Stratasys® Ltd.) was used for the fabrication of all specimens. This technique applies inkjet technology to deposit droplets of photopolymers that are then cured by UV light. We introduced the gradient in the specimens by creating grayscale images that were then converted into binary images using halftoning algorithms. The binary images worked as input files for bitmap 3D printing, informing the printer where to deposit which droplet of material. We used two commercially available materials, namely VeroCyan$^{TM}$ (RGD841, shore hardness (D) = 83–86) and Agilus30$^{TM}$ Black (FLX985, shore hardness (A) = 30–35) respectively as the hard and soft phases.

The standard dog-bone tensile test specimens (following JIS K 7161 (ISO 527-1) protocols for the tensile testing of polymer and plastics [44]) and single-edge notched uniaxial tensile test specimens with pre-existing cracks were used. The corresponding dimensions of both types of specimens are presented in Fig. 1. All groups had a symmetric gradient starting from a complete hard phase (*i.e.*, $\rho_h = 100\%$) at both sides of the specimens. The volume fraction of the hard phase gradually decreased (in a step-wise or continuous manner) to reach a pure soft phase in the center of structures (*i.e.*, $\rho_h = 0\%$). Based on our preliminary results, Young's modulus of the hard and soft phases were respectively 726.36 ± 59.77 MPa and 0.60 ± 0.05 MPa [45,37], meaning that the hard phase was more than 1000 times stiffer than the soft phase.

Two additional types of fracture specimens were fabricated by increasing the volume fraction of the hard phase in the middle of the specimens to $\rho_h = 20\%$ and $\rho_h = 40\%$ (Fig. 1g). These latter groups are referred to as 80-20-80 and 60-40-60. The pre-existing cracks were placed at the weakest region of the notched FGM specimens and spanned 20% of their widths.

Tensile test specimens with a sharp hard-soft-hard transition (*i.e.*, no gradient) were also created as a control group to enable comparison with FGM designs. All specimens (*i.e.*, notched or tensile) had an equal overall hard volume fraction of 50%.

In order to attach the specimens to the mechanical testing machine, they were designed with two extensions that were printed using the same hard material (Fig. 1) and were attached to two different types of custom-made aluminum grippers using aluminum pins. A mechanical testing machine (LLOYD instrument LR5K, loadcell = 5kN) was used to test both tensile and notched specimens in the displacement-controlled mode using a stroke rate of 2 mm/min. The time, force, and displacement were recorded at a sampling rate of 20 Hz.

The normal tensile stress was defined as $\sigma_t = F_t/A_t$, where $A_t = a_t \times t_t$ is the initial gauge cross section area. The thickness of the tensile specimens was $t_t = 4$ mm. The normal strain was calculated as $\varepsilon_t = u_{t,y}/L_t$, where $u_{t,y}$ is the longitudinal displacement and $L_t$ is the gauge length. Similarly, the stress of the notched specimens, $\sigma_f$, was defined as the ratio of force, $F_f$, to the effective cross-section area, $A_f = t_f \times (H_f - a_{f,0})$, where the out-of-plane thickness of the notched specimens, $t_f$, was 3 mm. The strain for these specimens was defined as $\varepsilon_f = u_{f,y}/L_f$, where $u_{f,y}$ is the displacement in the loading direction and $L_f$ is the initial free length between grippers. The Young's modulus, $E_t$, for the tensile tests (or stiffness of the notched specimen, $E_f$) was calculated using a moving regression algorithm with a bounding box of 0.02% and by finding the stiffest section of the loading curve. The ultimate tensile strength, $\sigma_{uts}$ (or maximum fracture stress, $\sigma_{f,max}$), was defined as the maximum stress. The elongation, $\varepsilon_{f,max}$ (or the maximum fracture strain, $\varepsilon_{f,max}$), was defined as the maximum strain at the end of the test. The toughness, $U_t$, (or the fracture energy, $U_f$, for the notched specimens) was measured by numerically integrating the area below the stress–strain curves until final rupture (the end of the test).

The digital image correlation (DIC) technique was used to measure the distribution of strains in the notched (5-steps and linear gradient) and tensile (abrupt transition, 5-steps, and linear) test specimens. For DIC measurements, a speckled black dot pattern was created on a white background on one side of the specimens. The DIC system was equipped with two digital cameras (4 MP with CMOS chip). The associated

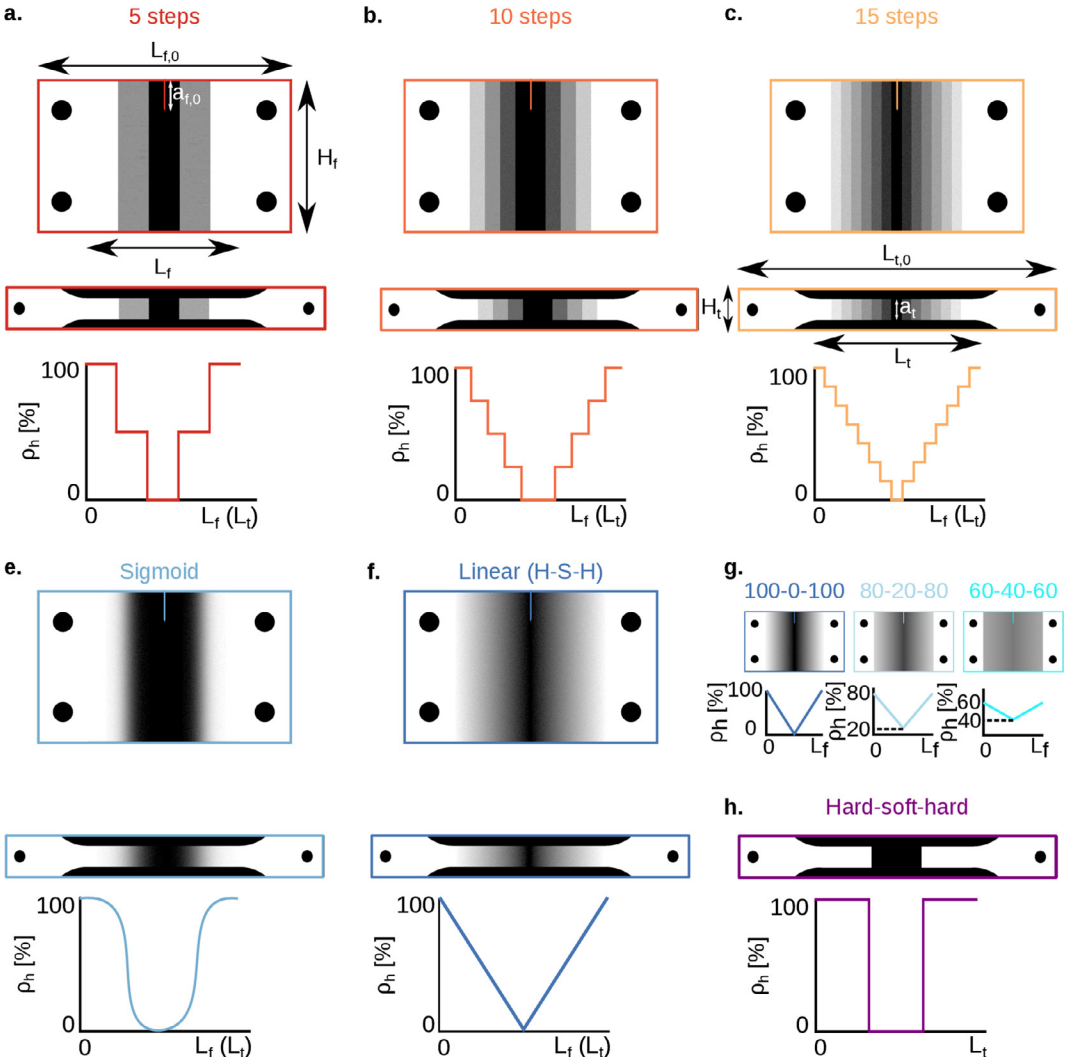


**Fig. 1.** A schematic view of dog-bone and notched specimens with stepwise and continuous gradients. In the case of the notched specimens, cracks were placed at the softest region of the specimens. For both fracture and tensile test specimens, three types of stepwise gradients, namely 5-steps (a), 10-steps (b), and 15-steps (c), and two types of continuous gradients, namely sigmoid (e) and linear (f), were considered. Three variations of the specimens with linear gradients were created that followed XX-YY-XX orders, where XX and YY refer to the volume fraction of the hard phase, $\rho_h$, at the top, middle, and bottom parts of these specimens. The values of XX and YY are listed in (g). Tensile specimens with an abrupt hard-soft transition were also created as a control group (h). The white and black pixels respectively represent the hard and soft phases. The dimensions of the notched specimens were as follows: $L_f$ = 75 mm, $H_f$ = 75 mm, $L_{f,0}$ = 100 mm, and $a_{f,0}$ = 15 mm (a). The geometrical parameters for the tensile specimens were: $L_t$ = 80 mm, $H_t$ = 20 mm, $L_{t,0}$ = 170 mm, and $a_t$ = 10 mm (c).

commercial software (Vic-3D 1, Correlated Solutions, SC, USA) was used to determine the strain distribution.

The fracture surfaces of both types of specimens (*i.e.*, notched and tensile) were analyzed using a digital microscope (Keyence® vhx-5000) at 200× magnifications with a zoom lens (VH-Z20T). Scanning electron microscopy (JSM-IT100, JEOL, Tokyo, Japan) with an electron beam energy of 10 kV and a magnification of 35,000× was used to capture and analyze the characteristics of the fracture surfaces of representative specimens in more detail.

We used atomic force microscopy (AFM, JPK Nanowizard 3, Berlin, Germany) with a NCHV probe (Bruker, USA) and a nominal spring constant of 40 N/m to locally measure the elastic modulus of the graded (*i.e.,* step-wise and continuous) and non-graded specimens. The post-processing steps were carried using the JPK SPM data processing software (JPK instruments, v6.1, Berlin, Germany). The calibration step was performed using the thermal noise method, resulting in a spring constant of 41.06 N/m and a sensitivity of 19.24 nm/V for the probe used in our experiments. The indentation curves were recorded by setting the force setpoint in the range of 1–4 μN, so as to obtain an indentation depth of ≈40 nm. The elastic modulus was determined by fitting the Sneddon contact mechanics model to the obtained indentation curves assuming the AFM tip to be a conical indenter with a tip radius of 8 nm (the nominal value). Three measurements for each region were performed.

The surface of the specimen was smoothenedd following a procedure suited for polymeric materials (Buehler polishing protocol): we first used SiC abrasive papers with decreasing grain sizes (*i.e.,* grids of 400, 800, 1200, 2500) followed by a two-step polishing using diamond (3 μm) and alumina (50 nm) particles in suspension. The surface preparation was performed under constant water irrigation using a MetaServ 250 (Buehler, US) machine. Nanoindentations experiments were carried out using a TI 950 Triboindenter (Bruker, US) equipped with a diamond conospherical probe with a tip radius of 20 μm. In order to capture the full interaction between the probe and the surface of the specimen, as required when indenting soft materials due to adhesion effects [46,47], a displacement-controlled load function was adopted. Starting in contact with the surface, the probe was first retracted 2 μm above the surface. After 10 s of holding time, the tip was pushed into

the specimen, reaching a maximum penetration depth of 1 μm. The probe was then held in place for 10 s after which it was retracted 2 μm above the surface. The loading and unloading speeds were both 100 nm/s. Such a test procedure enabled the quantification of the adhesion effects by measuring the jump-to-contact point (*i.e.,* when the probe gets in contact with the surface of the specimen during the approaching phase) as well as the pull-off force (*i.e.,* the maximum adhesive force during unloading). If the total pull-off force was higher than 5% of the maximum penetration load, the resulting load–displacement curves were analyzed using the Johnson-Kendal-Roberts (JKR) adhesion model [47]. Otherwise, the standard Oliver-Pharr method was applied [48]. The measurements were performed on a rectangular grid comprising 600 (*i.e.,* 30 × 20) locations that were equally spaced (500 μm apart in either direction).

We used X-ray photoelectron spectroscopy (XPS, ThermoFisher K-Alpha, Rockford, IL, USA) analysis to determine the chemical composition of the hard-soft composites. The parameters of the XPS analysis were as follows; X-ray gun settings: cathode at 12 kV, beam of 3 mA (for a 400 μm spot), flood gun settings: 1V, 100 μA, pressure when flood gun was on $= 5.10^{-7}$ mbar. For these analyses, an additional specimen (cuboid with the dimensions of 20 × 10 × 3.5 $mm^3$) with an abrupt hard-soft transition was 3D printed. Before testing, the support materials were carefully removed from the surfaces of the specimens. We used mechanical fixation to hold the specimen on the holder of the XPS machine during the measurements. The XPS analysis was performed along two scan lines which were across the transition from the hard to soft phases. Two individual points were measured further away from the transition zone, located in the hard or soft section of the specimen. We reported the average values of the atomic percentages of each element.

## 3. Results and discussion

The stress–strain curves measured for all tensile test specimens followed similar trends. In all cases, stress linearly increased until a sudden fracture occurred (Fig. 2a). From these results, one can divide the stress–strain behavior of these structures into two major categories. The first category includes those with linear or 15-steps gradients, while the specimens with an abrupt change in the mechanical properties, 5-step, 10-steps, and sigmoid gradients constitute the second category (Fig. 2a).

As expected, the strain distribution was not uniform along the length of the tensile test specimens both for graded and non-graded specimens and large strains were observed in the soft regions. The strain was highly concentrated in the middle of these tensile specimens particularly in the areas with a high amount of the soft phase (Fig. 2b, d and f). Furthermore, the strain distribution was smoother in the case of the specimens with linear gradients as compared to the specimens with sharp or stepwise transitions (Fig. 2b, d, and f).

The final fracture occurred within the gauge length and at the hard-soft interface for the cases with abrupt transitions and those with 5- and 10-steps gradients. However, in the case of the continuous and 15-steps gradients, the location of the fracture was in the middle of the specimens.

Specimens with linear gradients showed clear necking in the middle (Fig. 2f), while there was no clear necking for those with abrupt or stepwise gradients (Fig. 2b and d). The fracture surface was flat in all cases. That resulted in semi-elliptical cracks at the fracture surfaces of the specimens with linear gradients (Fig. 2g). The fracture surface of the specimens with an abrupt transition and 5-steps gradients were similar (Fig. 2c and e). The fracture surface on the hard side of those specimens contained soft material residues (Fig. 2c and e). Macroscopic cracks in the form of elliptical and semi-elliptical cracks were also observed close to the edges of the fracture surfaces in all tensile test specimens (Fig. 2c, e, and g).

Introducing a linear gradient increased Young's modulus by a factor of 3 and the ultimate strength by a factor of 1.75 as compared to the control group, namely an abrupt hard-soft-hard transition (Fig. 3a and b). However, the trade-off for the implementation of these linear graded materials is that the toughness and elongation dropped respectively by 35% and 65% as compared to the control group (Fig. 3c and d). The specimens with sigmoid gradients were the only groups that had toughness and elongation values comparable to those of the control group while exhibiting higher values of the ultimate tensile strength and Young's modulus (Fig. 3). Since the elongation of purely soft and hard phases are very different, assigning a higher portion of the soft phase to these FGM composites could increase the elongation of theses composites, which is what happened in the specimens with sigmoid gradients.

Among the specimens with stepwise gradients, those with 15 steps showed a significantly higher (≈ 2-folds) Young's modulus (Fig. 3a) and a higher ultimate strength (Fig. 3b) as compared to the other stepwise graded specimens. Similar to the cases with linear gradients, specimens with 15-steps gradients did not exhibit higher values of the toughness and elongation. Moreover, there was a very sharp change in the mechanical properties of the specimens with 15-steps gradients on the one hand and those with 5- or 10-steps gradients on the other hand. This suggests that the mechanical properties of the stepwise FGMs highly depend on the number of steps (or the step sizes). One could, therefore, use computational design tools including optimization algorithms to design FGMs with much-improved properties for specific applications at hand.

Notched stepwise (*i.e.*, 5-, 10- and 15-steps) and continuous (linear 100-0-100, and sigmoid) specimens showed similar trends to what was observed for the tensile test specimens (Fig. 4a). In particular, the stress–strain curves showed a linear increase at the initial stage. A high level of deformation was required to open the cracks. Crack blunting was also observed before and after the start of crack propagation (Fig. 4b and c). After reaching the maximum fracture force (stress), the crack started to propagate in the specimens. Although large deformations were observed on the other side of the specimens (the side without a crack) before and after the start of crack propagation, the crack growth always started from the crack tip and moved along a straight path in the middle of the specimens (Fig. 4b and c).

DIC images clearly showed the presence of strain concentrations in front of the crack tip and at the middle of the specimens (Fig. 4b and c). The size of the strain concentration zone grew as the specimens were stretched further (Fig. 4b and c). The high-strain zones were smaller for the specimens with a linear gradient as compared to those with a 5-steps gradient (Fig. 4b and c). No stress concentrations were observed far away from the cracks (Fig. 4b, c).

The concentration of micro- and macrocracks was high close to the crack tip both for the specimens with a linear gradient and those with 5-steps gradients (zones I and II in Fig. 4d and e). Moreover, the cracks propagated to the boundaries of the specimens (zone II in Fig. 4d and e) to reach free surfaces with a minimum level of energy. The macroscopic elliptical and semi-elliptical cracks were also observed in the middle of the fracture surface of the specimens with 5-step gradients (zone III in Fig. 4d). The fracture surface was free of microcracks close to the side that did not have a pre-existing crack (zone IV in Fig. 4d and e).

The stiffness and fracture stress of the specimens with linear and 15-steps gradients were higher (up to ≈ 2-folds) as compared to the other cases (Fig. 5a, b, e, and f). The fracture toughness values measured for all specimens were of the same order of magnitude with slightly higher values for those with linear and 15-steps gradients (Fig. 5c–f). However, specimens with 5-steps, 10-steps, and sigmoid gradients showed higher values of the maximum fracture strain (Fig. 5d).

As the fracture properties of these specimens highly depend on the amount of hard (soft) materials present in front of the crack tip, we increased the hard volume fraction in those regions by a factor of 2 and 4. To keep the overall volume fraction of the hard phase constant in all specimens, we linearly increased the volume fraction of the hard phase

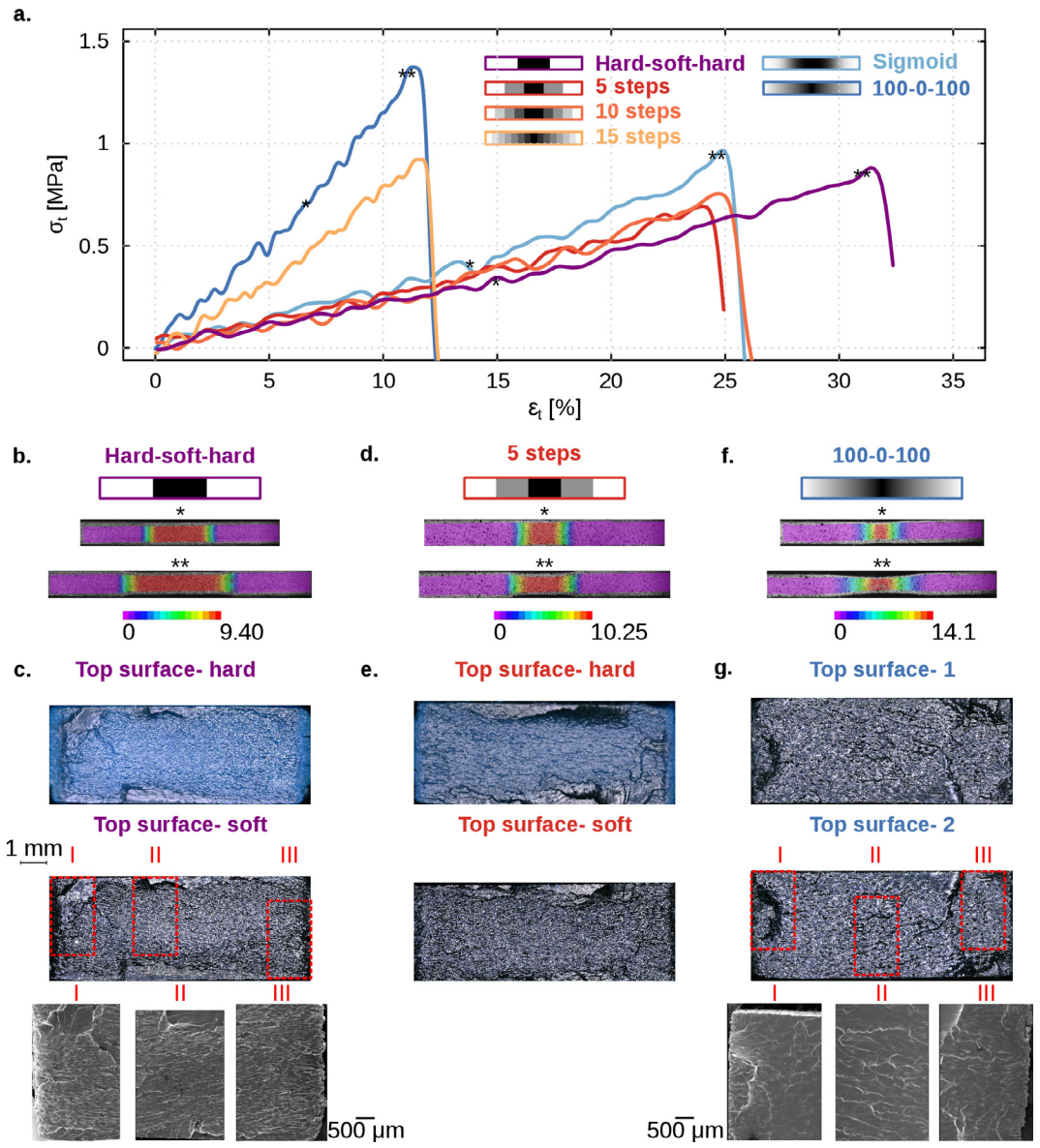


**Fig. 2.** (a) Typical stress–strain curves of the tensile test specimens with graded or non-graded transitions. Full-field strain measurement using DIC of the specimens with an abrupt sharp hard-soft-hard transition (b), 5-steps (d), and linear (f) transition functions. DIC images show the distribution of the von Misses strain values before the maximum load is reached (*) and at the maximum load (**). Digital microscopy (200X magnifications) and the corresponding SEM images (35,000X magnifications) of the fracture surface of the specimens with a sharp hard-soft-hard transition, 5-steps, and linear gradients are presented in sub-figures (c), (e), and (g), respectively. The scale bars for the digital microscopy and SEM images are placed next to the corresponding images. The hard phase is shown using white pixels, while the soft phase is in black.

to respectively 80% and 60% towards the end of the specimens (*i.e.*, the 80-20-80 and 60-40-60 groups). Increasing the volume fraction of the hard phase to 20% (*i.e.*, the 80-20-80 group) resulted in a 2.5-folds increase in the stiffness and a 2-folds increase in the fracture energy and fracture stresses as compared to the 100-0-100 specimens (Fig. 5a-c, e-f). Increasing the hard volume fraction to 40% (*i.e.*, the 60-40-60 group) resulted in a 9-folds increase in the stiffness, a 4-folds increase in the fracture stress, and a 5-folds increase in the fracture energy (Fig. 5a-c, e-f) as compared to the 100–0-100 group. The fracture surfaces of these specimens (*i.e.*, 80-20-80 and 60-40-60 groups) also showed a continuous microcrack distribution along the crack path and perpendicular to the plane of the loading direction (zones I to IV in Fig. 5f, g). In contrast to the specimens that had pure soft materials in the middle (*i.e.*, 5-steps and 100-0-100), microcracks in the case of the 80-20-80 and 60-40-60 groups were found all over the fracture surface (zone IV in Fig. 4d–g).

The AFM results of the specimens with 5-steps gradients suggested little variations in the elastic moduli measured within the transition zone: the local elastic modulus close to the hard phase was 537 ± 110.07 MPa while it was 490 ± 75.29 MPa at a location close to the soft phase of specimens. The AFM results of the specimens with a linear gradient showed a nonlinear change in the local values of the elastic moduli (Fig. 6a). We observed a similar trend from the nanoindentation experiments (Fig. 6b and c), although the elastic moduli measured from the AFM measurements were slightly higher than those from the nanoindentation tests. This could be due to the fact that we performed the AFM measurements at a depth of about 40 nm. As we did not perform any surface modification before AFM testing, this depth could be below the surface roughness of the specimen. Nevertheless, both methods showed a nonlinear change of the elastic modulus in the graded specimens. This suggests that although the change of the hard volume fraction was defined linearly, the change in the elastic moduli

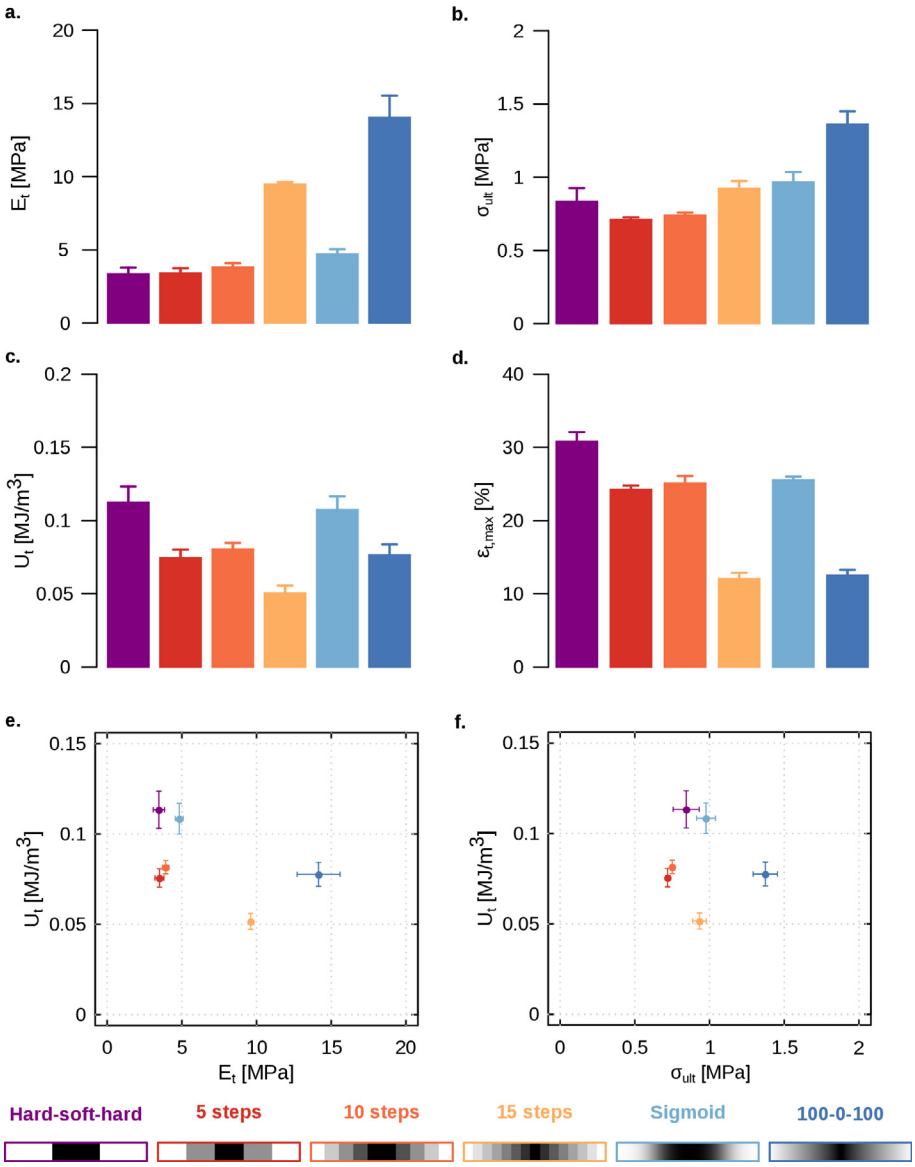


**Fig. 3.** Bar-plots comparing the tensile mechanical properties of the specimens from different experimental groups. The mechanical properties include the Young's modulus (a), ultimate stress (b), toughness (c), and elongation (d). The Ashby plots of the toughness vs. Young's modulus (e) and toughness vs. ultimate tensile strength (f) are also presented. The data points indicate the mean and standard deviations of the values measured for each experimental group.

was not necessarily linear (Fig. 6a–c). This can be due to the mixing of the hard and soft particles at the level of individual voxels (*i.e.,* 40 μm) deposited by the 3D printer. Therefore, further analyses are required to determine the best strategy for controlling the small-scale values of the elastic moduli in such FGMs.

We found five main elements from our XPS measurements in the structure of the hard (and soft) polymers including C (C1s), O (O1s), N (N1s), Ca (Ca2p) and S (Si2p). The binding energy for the hard and soft polymers showed a similar trend (Fig. 6b) with a peak at ≈286 eV that corresponded to the C–O–C chemical state. The hard phase showed a slightly higher C1s atomic percentage as compared to the soft phase (Fig. 6b and c, and Table 1). Moreover, the hard polymer contained slightly more silicon than nitrogen in its composition (Fig. 6b and c, and Table 1). In the soft phase, however, the nitrogen concentration was slightly higher than silicon (Fig. 6b and c, and Table 1). We did not observe a significant change in the oxygen or carbon contents at the interface of the hard-soft composites (Fig. 6c). The atomic percentages of N and Si slightly increased at the transition line from the hard to the soft material (Fig. 6c).

The characteristics of the fracture surface of FGMs tested in this study is similar to our previous results. Previously, we had investigated the crack propagation in two dissimilar materials (*i.e.,* from hard to soft) [49] as well as in bio-inspired composites with heterogeneous dispersions of hard and soft particles [37]. Comparing the results of this study with those of our previous ones suggests that increasing the hard volume fraction in front of the crack tip can activate other toughening mechanisms, such as crack bridging in FGMs. In addition, the combination of functional gradients with other natural design paradigms, such as hierarchical length-scaling, may further improve the properties of these FGMs. Furthermore, introducing other geometry-based toughening mechanisms (*e.g.,* brick-and-mortar arrangements) similar to those found in hard tissues (*e.g.,* nacre or bone) can push the fracture properties of these materials to even higher values.

These observations suggest that by rationally designing these FGM composites, one can significantly outperform the mechanical properties and fracture behavior of conventional composites. This is an important approach that could benefit several engineering disciplines including bioengineering [50], soft robotics [51,52], and aerospace. In addition,

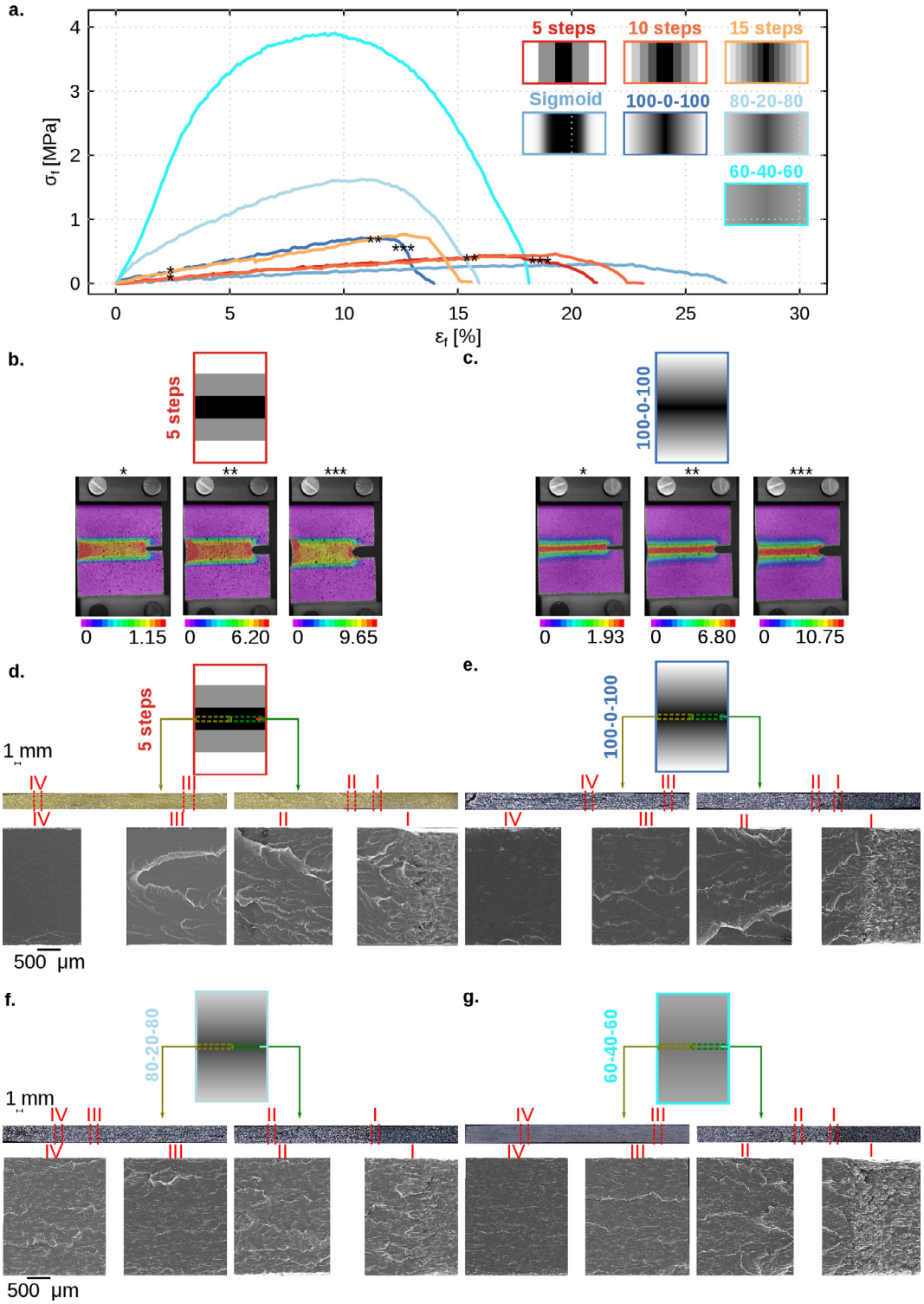


**Fig. 4.** (a) Typical stress–strain curves of the notched specimens with different types of gradients. Full-field strain measurement using DIC for the specimens with a 5-steps (b) and linear (c) transition function. DIC images show the von Misses strain before the maximum load (*), at the maximum load (**), and after the maximum load (***). Digital microscopy (200X magnifications) and the corresponding SEM (35,000X magnifications) images of the fracture surface of the specimens with 5-step gradients are presented in sub-figure (d). Similar digital microscopy and SEM images for the linear XX-YY-XX gradients are presented in sub-figures (e), (f), and (g). XX and YY refer to the volume fraction of the hard phase, $\rho_h$, at the top, middle, and bottom parts of the specimens. The values of XX and YY are presented in the corresponding sub-figures. The scale bars for the digital microscopy and SEM images are placed at the top and bottom of the corresponding images, respectively. The hard phase is shown using white pixels, while the soft phase is in black.

such design strategies can be implemented in the design and fabrication of advanced cellular materials such as mechanical metamaterials [45,53–57] whose properties originate from their design at the micro-level to achieve new properties and functionalities. Understanding the behavior of functionally graded designs under different loading conditions such as fatigue [58] and impact [59] are the other research lines for future investigations.

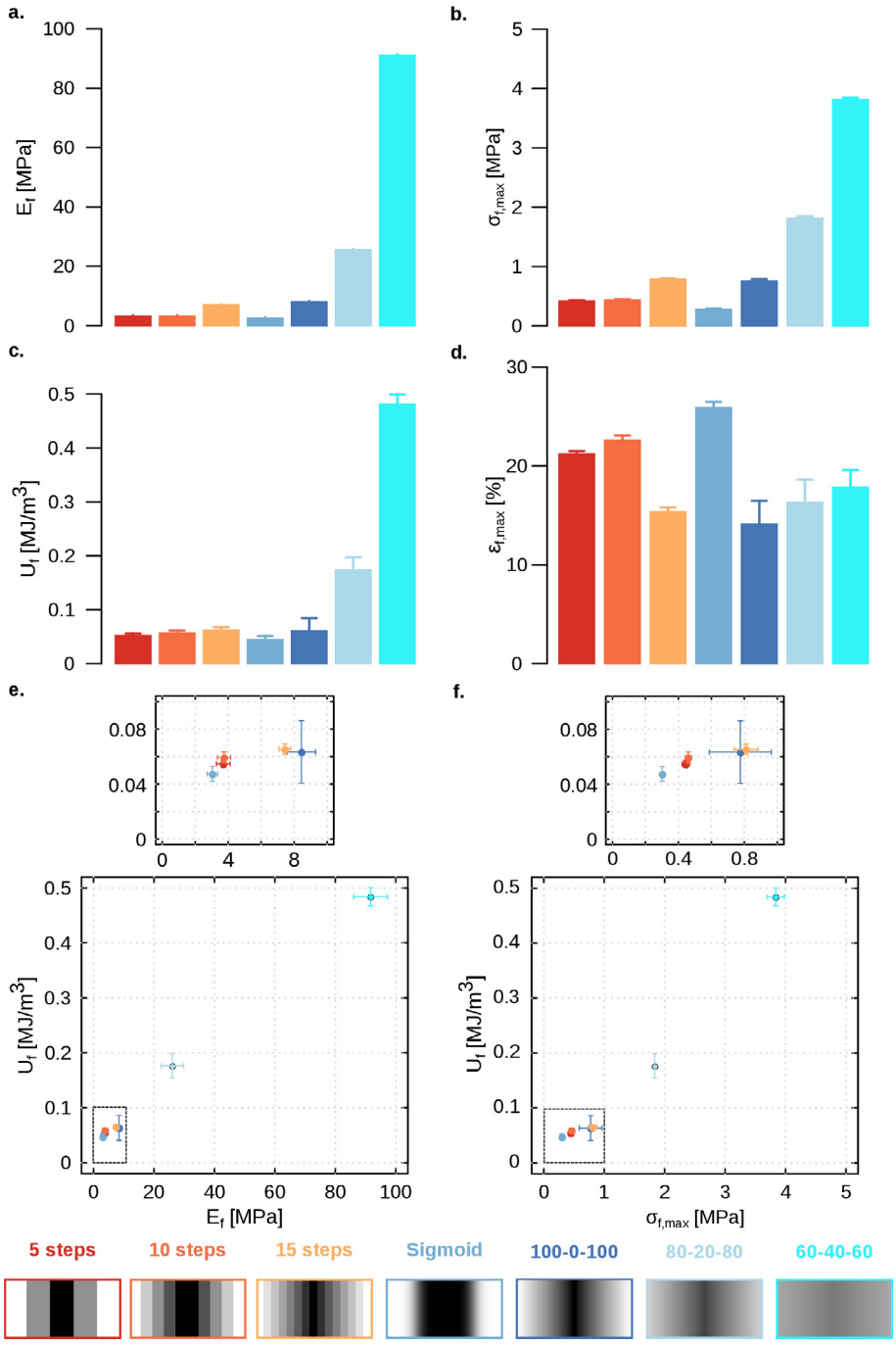


**Fig. 5.** Bar-plots comparing the fracture properties of the notched specimens belonging to seven experimental groups. The properties include the stiffness (a), fracture stress (b), fracture energy (c), and final fracture strain (d). Ashby plots that compare the fracture energy vs. stiffness and the fracture energy vs. fracture stress are presented respectively in sub-figures (e) and (f). The plots on top of the Ashby plots show the zoomed-in views of the regions specified in the main plots. Each data point indicates the mean and standard deviations of the values measured for an experimental group.

## 4. Conclusion

In summary, we studied the mechanical properties and fracture behavior of functionally graded hard-soft composites. We discussed some of the important failure mechanisms involved in the fracture of such designs. FGMs with a continuous gradient (*i.e.*, linear) showed higher Young's moduli (≈3-folds) (and ≈2-folds increase in the stiffness) and ultimate strengths (≈2-folds) (and ≈2-folds in the fracture stress) as compared to those with stepwise gradients (*i.e.*, 5-steps). The trade-off is a decrease in the elongation (≈2-folds drop) and fracture resistance (≈1.5-folds drop). In addition, we found that by engineering the properties of the FGMs and incorporating a higher amount of hard material in front of the crack tip, it is possible to tune the properties of FGMs. From the micro-mechanical characterization viewpoint, we observed that the elastic moduli of FGMs fabricated by bitmap 3D printing do not necessarily follow the rule of mixtures. From the chemical composition viewpoint, we found no substantial change in the elemental constituents of the commercial hard and soft polymers used in this study.

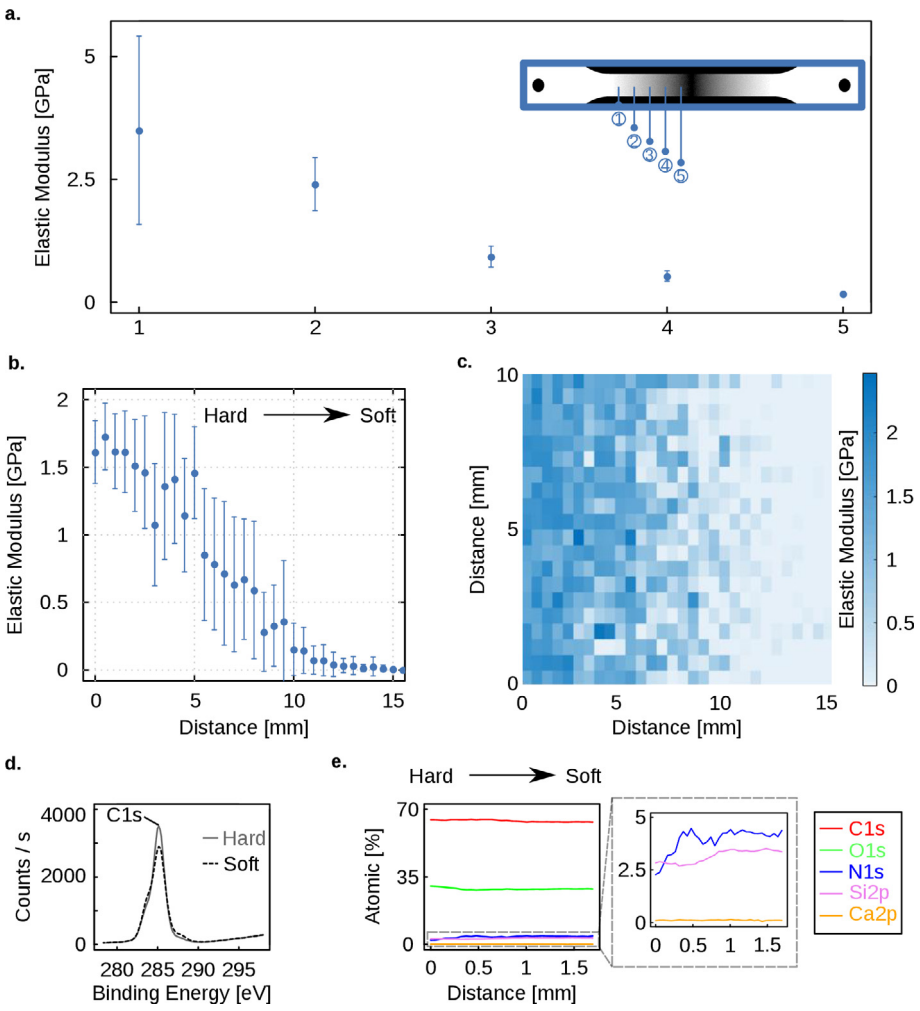


**Fig. 6.** The elastic moduli obtained from the AFM (a) and nano-indentation (b) experiments for the specimens with a linear gradient. The locations at which the AFM measurement were performed are shown in the inset of subfigure (a). The 2D heatmap plot (c) shows the distribution of the elastic moduli obtained from the nanoindentation experiments in the specimens with a linear gradient. The concentration of carbon in the monolithic hard and soft polymers had a peak at about 286 eV (d). The atomic percentage profiles measured by XPS for the other elements along a line from the hard-soft connection (e).

**Table 1**
The atomic percentages of the hard and soft polymers measured using XPS.

| | Hard | Soft |
|---|---|---|
| C1s | 64.61 | 63.858 |
| O1s | 30.12 | 28.63 |
| N1s | 2.435 | 4.405 |
| Ca2p | 0.125 | 0.12 |
| Si2p | 2.71 | 3.315 |

## CRediT authorship contribution statement

**M.J. Mirzaali:** Conceptualization, Methodology, Formal analysis, Resources, Writing - original draft, Supervision, Visualization, Writing - review & editing. **A Herranz de la Nava:** Conceptualization, Methodology, Formal analysis, Visualization, Writing - review & editing. **D. Gunashekar:** Conceptualization, Methodology, Formal analysis, Writing - review & editing. **M. Nouri-Goushki:** Formal analysis, Writing - review & editing. **R.P.E. Veeger:** Formal analysis, Writing - review & editing. **Q. Grossman:** Formal analysis, Writing - review & editing. **L. Angeloni:** Formal analysis, Resources, Writing - review & editing. **M.K. Ghatkesar:** Resources, Writing - review & editing. **L.E. Fratila-Apachitei:** Resources, Writing - review & editing. **D. Ruffoni:** Resources, Writing - original draft, Supervision, Writing - review & editing. **E.L. Doubrovski:** Conceptualization, Methodology, Resources, Writing - original draft, Supervision, Writing - review & editing. **A.A. Zadpoor:** Conceptualization, Resources, Writing - original draft, Supervision, Writing - review & editing.

## Declaration of Competing Interest

The authors declare that they have no known competing financial interests or personal relationships that could have appeared to influence the work reported in this paper.

## Acknowledgments

This research was conducted on a Stratasys® Objet350 Connex3™ printer through the Voxel Print Research Program. This program is an exclusive partnership with Stratasys Education, that enhances the value of 3D printing as a powerful platform for experimentation, discovery and innovation, for more information contact: academic.research@stratasys.com.

## References

[1] Chen Po-Yu, McKittrick Joanna, Meyers Marc André. Biological materials: functional adaptations and bioinspired designs. Prog Mater Sci 2012;57(8):1492–704.

[2] Dunlop John WC, Weinkamer Richard, Fratzl Peter. Artful interfaces within biological materials. Mater Today 2011;14(3):70–8.
[3] Smith Bettye L, Schäffer Tilman E, Viani Mario, Thompson James B, Frederick Neil A, Kindt Johannes, et al. Molecular mechanistic origin of the toughness of natural adhesives, fibres and composites. Nature 1999;399(6738):761.
[4] Dawson Colin, Vincent Julian FV, Rocca Anne-Marie. How pine cones open. Nature 1997;390(6661):668.
[5] Zaslansky Paul, Friesem Asher A, Weiner Steve. Structure and mechanical properties of the soft zone separating bulk dentin and enamel in crowns of human teeth: insight into tooth function. J Struct Biol 2006;153(2):188–99.
[6] Benjamin Michael, Kumai Tsukasa, Stefan Milz BM, Boszczyk AA Boszczyk, Ralphs JR. The skeletal attachment of tendonsâ€"tendon â€enthesesâ€™. Comp Biochem Physiol Part A Mol Integr Physiol 2002;133(4):931–45.
[7] Miserez A, Schneberk T, Sun C, Zok FW, Waite JH. The transition from stiff to compliant materials in squid beaks. Science 2008;319(5871):1816–9.
[8] Bruce R, Martin. Porosity and specific surface of bone. CRC Crin Rev Biomed Engng 1984;10:179–222.
[9] Gupta HS, Schratter S, Tesch W, Roschger P, Berzlanovich A, Schoeberl T, et al. Two different correlations between nanoindentation modulus and mineral content in the bone–cartilage interface. J Struct Biol 2005;149(2):138–48.
[10] Wang Fuyou, Ying Zhang, Duan Xiaojun, Tan Hongbo, Yang Bin, Guo Lin, et al. Histomorphometric analysis of adult articular calcified cartilage zone. J Struct Biol 2009;168(3):359–65.
[11] Benjamin M, Ralphs JR. Tendons and ligaments-an overview. Histol Histopathol 1997;12(4):1135–44.
[12] Jensen Gail M. Biomechanics of the lumbar intervertebral disk: a review. Phys Ther 1980;60(6):765–73.
[13] Robert F Ker. The design of soft collagenous load-bearing tissues. J Exp Biol 1999;202(23):3315–24.
[14] Hoemann Caroline D, Lafantaisie-Favreau Charles-Hubert, Lascau-Coman Viorica, Chen Gaoping, Guzmán-Morales Jessica. The cartilage-bone interface. J knee Surg 2012;25(02):085–98.
[15] Alice J, Fox Sophia, Bedi Asheesh, Rodeo Scott A. The basic science of articular cartilage: structure, composition, and function. Sports Health 2009;1(6):461–8.
[16] Ahankari Sandeep S, Kar Kamal K. Functionally graded composites: Processing and applications. Composite Materials. Springer; 2017. p. 119–68.
[17] Bohidar Shailendra Kumar, Sharma Ritesh, Ranjan Mishra Prabhat. Functionally graded materials: a critical review. Int J Res 2014;1(4):289–301.
[18] Henriques B. Inhomogeneous materials perform better: functionally graded materials for biomedical application. J Powder Met Min 2013;2(3):1–2.
[19] Khoshgoftar MJ, Mirzaali MJ, Rahimi GH. Thermoelastic analysis of non-uniform pressurized functionally graded cylinder with variable thickness using first order shear deformation theory (fsdt) and perturbation method. Chin J Mechan Eng 2015;28(6):1149–56.
[20] Naebe Minoo, Shirvanimoghaddam Kamyar. Functionally graded materials: a review of fabrication and properties. Appl Mater Today 2016;5:223–45.
[21] Kokkinis Dimitri, Bouville Florian, Studart André R. 3d printing of materials with tunable failure via bioinspired mechanical gradients. Adv Mater 2018;30(19):1705808.
[22] Studart Andre R. Biological and bioinspired composites with spatially tunable heterogeneous architectures. Adv Funct Mater 2013;23(36):4423–36.
[23] Liu Huanhuan, Yang Long, Zhang Erchen, Zhang Rui, Cai Dandan, Zhu Shouan, Ran Jisheng, Bunpetch Varitsara, Cai Youzhi, Chin Heng Boon, et al. Biomimetic tendon extracellular matrix composite gradient scaffold enhances ligament-to-bone junction reconstruction. Acta Biomater 2017;56:129–40.
[24] Stella John A, Dâ€™Amore Antonio, Wagner William R, Sacks Michael S. On the biomechanical function of scaffolds for engineering load-bearing soft tissues. Acta Biomater 2010;6(7):2365–81.
[25] Tellado Sonia Font, Balmayor Elizabeth R, Van Griensven Martijn. Strategies to engineer tendon/ligament-to-bone interface: biomaterials, cells and growth factors. Adv Drug Deliv Rev 2015;94:126–40.
[26] Seidi Azadeh, Ramalingam Murugan, Elloumi-Hannachi Imen, Ostrovidov Serge, Khademhosseini Ali. Gradient biomaterials for soft-to-hard interface tissue engineering. Acta Biomater 2011;7(4):1441–51.
[27] Garg Tarun, Singh Onkar, Arora Saahil, Murthy RSR. Scaffold: a novel carrier for cell and drug delivery. Crit Rev Ther Drug Carrier Syst 2012;29(1):1–63.
[28] Soares Rosane MD, Siqueira Nataly M, Prabhakaram Molama P. and Seeram Ramakrishna. Electrospinning and electrospray of bio-based and natural polymers for biomaterials development. Mater Sci Eng, C 2018.
[29] Wang Zhengzhi, Shi Xiaoming, Huang Houbing, Yao Chenmin, Xie Wen, Huang Cui, et al. Magnetically actuated functional gradient nanocomposites for strong and ultra-durable biomimetic interfaces/surfaces. Mater Horiz 2017;4(5):869–77.
[30] Wang Zhengzhi. Slanted functional gradient micropillars for optimal bioinspired dry adhesion. ACS Nano 2018;12(2):1273–84.
[31] Wang Zhengzhi, Wang Kun, Huang Houbing, Cui Xiao, Shi Xiaoming, Ma Xingqiao, Li Bei, Zhang Zuoqi, Tang Xuhai, Chiang Martin YM. Bioinspired wear-resistant and ultradurable functional gradient coatings. Small 2018;14(41):1802717.
[32] Hutmacher Dietmar W. Scaffold design and fabrication technologies for engineering tissuesâ€"state of the art and future perspectives. J Biomater Sci Polym Ed 2001;12(1):107–24.
[33] Binder Kyle W, Allen Arthur J, Yoo James J, Atala Anthony. Drop-on-demand inkjet bioprinting: a primer. Gene Ther Regul 2011;6(01):33–49.
[34] Murphy Sean V, Atala Anthony. 3d bioprinting of tissues and organs. Nat Biotechnol 2014;32(8):773.
[35] Doubrovski EL, Tsai Elizabeth Yinling, Dikovsky Daniel, Geraedts Jo MP, Herr Hugh, Oxman Neri. Voxel-based fabrication through material property mapping: A design method for bitmap printing. Comput Aided Des 2015;60:3–13.
[36] Bracaglia Laura G, Smith Brandon T, Watson Emma, Arumugasaamy Navein, Mikos Antonios G, Fisher John P. 3d printing for the design and fabrication of polymer-based gradient scaffolds. Acta Biomater 2017;56:3–13.
[37] Mirzaali MJ, Edens ME, Herranz A, de la Nava S, Janbaz P Vena, Doubrovski EL, et al. Length-scale dependency of biomimetic hard-soft composites. Sci Rep 2018;8(1):12052.
[38] Zhang Bin, Luo Yichen, Ma Liang, Gao Lei, Li Yuting, Xue Qian, Yang Huayong, Cui Zhanfeng. 3D bioprinting: an emerging technology full of opportunities and challenges. Bio-des. Manuf. 2018;1(1):2–13. https://doi.org/10.1007/s42242-018-0004-3.
[39] Loh Giselle Hsiang, Pei Eujin, Harrison David, Monzon Mario D. An overview of functionally graded additive manufacturing. Addit Manuf 2018;23:34–44.
[40] Kieback B, Neubrand A, Riedel H. Processing techniques for functionally graded materials. Mater Sci Eng A 2003;362(1–2):81–106.
[41] Rasheedat M Mahamood, Esther T Akinlabi, Mukul Shukla, Sisa Pityana. Functionally graded material: an overview; 2012.
[42] Talreja Ramesh, Chandra Veer Singh. Damage and failure of composite materials. Cambridge University Press; 2012.
[43] Valmik Bhavar, Prakash Kattire, Sandeep Thakare, RKP Singh, et al. A review on functionally gradient materials (fgms) and their applications. In IOP Conference Series: Materials Science and Engineering, volume 229, page 012021. IOP Publishing; 2017.
[44] K JIS. 7161-1994: Plasticsâ€"determination of tensile propertiesâ€"part 1: General principles. Japanese Standards Association; 1994.
[45] Mirzaali MJ, Caracciolo A, Pahlavani H, Janbaz S, Vergani L, Zadpoor AA. Multi-material 3d printed mechanical metamaterials: Rational design of elastic properties through spatial distribution of hard and soft phases. Appl Phys Lett 2018;113(24). 241903.
[46] Ebenstein Donna M, Wahl Kathryn J. A comparison of jkr-based methods to analyze quasi-static and dynamic indentation force curves. J Colloid Interface Sci 2006;298(2):652–62.
[47] Kohn Julie C, Ebenstein Donna M. Eliminating adhesion errors in nanoindentation of compliant polymers and hydrogels. J Mech Behav Biomed Mater 2013;20:316–26.
[48] Warren Carl Oliver and George Mathews Pharr. An improved technique for determining hardness and elastic modulus using load and displacement sensing indentation experiments. J Mater Res 1992;7(6):1564–83.
[49] Mirzaali Mohammad J, de la Nava Alba Herranz, Gunashekar Deepthi, Nouri-Goushki Mahdyieh, Doubrovski Eugeni, Zadpoor Amir A, et al. Fracture behavior of bio-inspired functionally graded soft–hard composites made by multi-material 3d printing: the case of colinear cracks. Materials 2019;12(17):2735.
[50] Mehrali Mehdi, Shirazi Farid Seyed, Mehrali Mohammad, Metselaar Hendrik Simon Cornelis, Kadri Nahrizul Adib Bin, Osman Noor Azuan Abu. Dental implants from functionally graded materials: dental Implants from FGM. J Biomed Mater Res Part A Off J Soc Biomater Jap Soc Biomater Austral Soc Biomater Kor Soc Biomater 2013;101(10):3046–57. https://doi.org/10.1002/jbm.a.v101.1010.1002/jbm.a.34588.
[51] Rob BN Scharff, Rens M Doornbusch, Xander L Klootwijk, Ajinkya A Doshi, Eugeni L Doubrovski, Jun Wu, Jo MP Geraedts, and Charlie CL Wang. Color-based sensing of bending deformation on soft robots. In 2018 IEEE International Conference on Robotics and Automation (ICRA), 1–7. IEEE; 2018.
[52] Schaffner Manuel, Faber Jakob A, Pianegonda Lucas, Rühs Patrick A, Coulter Fergal, Studart André R. 3d printing of robotic soft actuators with programmable bioinspired architectures. Nat Commun 2018;9(1):878.
[53] Zadpoor Amir A. Mechanical meta-materials. Mater Horiz 2016;3(5):371–81.
[54] Janbaz S, Bobbert FSL, Mirzaali MJ, Zadpoor AA. Ultra-programmable buckling-driven soft cellular mechanisms. Mater Horiz 2019.
[55] Wang Yu, Gao Jie, Luo Zhen, Brown Terry, Zhang Nong. Level-set topology optimization for multimaterial and multifunctional mechanical metamaterials. Eng Optim 2017;49(1):22–42.
[56] Chen Da, Zheng Xiaoyu. Multi-material additive manufacturing of metamaterials with giant, tailorable negative poissonâ€™s ratios. Scient Rep 2018;8.
[57] Kuang Xiao, Jiangtao Wu, Chen Kaijuan, Zhao Zeang, Ding Zhen, Fengjingyang Hu, et al. Grayscale digital light processing 3d printing for highly functionally graded materials. Sci Adv 2019;5(5):eaav5790.
[58] Dorcas V. Kaweesa and Nicholas A Meisel. Quantifying fatigue property changes in material jetted parts due to functionally graded material interface design. Addit Manuf 2018;21:141–9.
[59] Mueller Jochen, Shea Kristina. Stepwise graded struts for maximizing energy absorption in lattices. Extreme Mech Lett 2018;25:7–15.